C. R. Physique 11 (2010) 510–518

Contents lists available at ScienceDirect

Comptes Rendus Physique

www.sciencedirect.com

Terahertz electronic and optoelectronic components and systems

THz imaging techniques for nondestructive inspections

Techniques d'imagerie térahertz pour l'analyse industrielle non destructive

Kodo Kawase [a,b,*], Takayuki Shibuya [a,b], Shin'ichiro Hayashi [b], Koji Suizu [a]

[a] *Nagoya University, Furocho, Nagoya 464-8603, Japan*
[b] *RIKEN, 519-1399 Aramaki-aoba, Sendai 980-0845, Japan*

ARTICLE INFO

Keywords:
Terahertz imaging
Terahertz tomography
Metallic mesh sensor
Nondestructive testing

Mots-clés :
Imagerie térahertz
Tomographe THz
Capteur de grille métallique
Analyse industrielle non destructive

ABSTRACT

We have suggested a wide range of real-life applications using novel terahertz imaging techniques. A high-resolution terahertz tomography has been demonstrated by ultra short terahertz pulses using optical fiber and a nonlinear organic crystal. We also describe a nondestructive inspection system that can monitor the soot distribution in a ceramic filter using millimeter-to-terahertz wave computed tomography. Further, we report on the thickness measurement of very thin films using high-sensitivity metal mesh filter. These techniques are directly applicable to the nondestructive testing in industries.
© 2010 Published by Elsevier Masson SAS on behalf of Académie des sciences.

RÉSUMÉ

Nous proposons un grand nombre d'applications industrielles variées de nouveaux systèmes d'imagerie THz. Tout d'abord, nous avons construit un tomographe THz de très haute résolution, en employant un laser à fibre délivrant des impulsions optiques ultra-brèves qui éclairent un cristal non linéaire pour générer les signaux THz. Nous avons étendu la tomographie à l'inspection tri-dimensionnelle, par exemple de la répartition de la suie dans des filtres céramiques pour l'automobile, réalisée ici avec des ondes millimétriques. Enfin, nous décrirons la mesure de l'épaisseur de films très minces placées sur des grilles métalliques. Toutes ces techniques sont directement applicables au contrôle non destructif pour l'industrie.
© 2010 Published by Elsevier Masson SAS on behalf of Académie des sciences.

1. Introduction

Terahertz (THz) waves have the property of being able to pass through various objects, such as paper, vinyl, plastics, textiles, ceramics, semiconductors, lipids and powders, just like radio waves. THz waves are also able to image substances, just like X-rays, although they do not present risks of irradiation. The property of THz wave lies in moderate transmission and moderate absorption. Whereas X-rays sometimes render objects invisible because of their excessive strength of penetration, THz waves make things that cannot be seen with X-rays visible, because their strength of penetration is weaker. Metaphorically speaking, characters written with faint-colored ink on paper cannot be seen under strong light, but they become visible when viewed under moderate illumination. The ability of the THz wave to pass through many packaging materials will allow the nondestructive and noninvasive inspections for industries. Our group has been conducting research

* Corresponding author at: Nagoya University, Furocho, Nagoya 464-8603, Japan.
E-mail address: kawase@nuee.nagoya-u.ac.jp (K. Kawase).

1631-0705/$ – see front matter © 2010 Published by Elsevier Masson SAS on behalf of Académie des sciences.
doi:10.1016/j.crhy.2010.04.003

activities in several directions within the THz field. We have been developing novel widely tunable THz-wave sources using nonlinear crystals, and we suggested a whole range of real-life applications (e.g. [1]).

Among our research activities for applications, here we introduce: 1) Time of flight THz reflection tomography for multi-layered thin coatings; 2) THz computed tomography (CT) for the inspection of soot distribution in a ceramic filter; 3) Metal mesh sensor for the measurements of molecular bindings or thin film thickness. Although still at the beginning of a long road, the applications of THz waves have started to make visible progress and the results shown here represent a part of our contribution to the field. A whole range of other applications for industrial quality testing are underway in many research groups around the world, and are already receiving much interest both from physics investigators and from those specific communities.

2. High-resolution time-of-flight terahertz tomography using a femtosecond fiber laser

Since the electromagnetic field of the sub-picosecond terahertz pulses is measured directly with THz time domain spectroscopy (THz-TDS), the multilayered structure of a sample can be imaged by detecting the echo pulses reflected from each layer [2,3]. This technique is valuable in industry because the unique transmission characteristics of terahertz waves enables the inspection of multilayered paints in industrial products or tablet coatings [4,5], which are not measurable with optical coherence tomography (OCT) based on an optical light source [6].

As restricted by the temporal duration of the terahertz pulses used, the conventional axial resolution of terahertz tomography remains a few tens of microns, although an attempt to improve the axial resolution of time-of-flight measurements has been reported. In the technique described here [7], a terahertz interferometer was added to the reflection-type THz-TDS configuration to attain a resolution of 12.5 μm. Although this method has proven effective as a profilometer, it had not been investigated as a tomography system whereby multilayered structures are imaged. The common $\sim$10 μm thickness of paints in various industrial products and the stratum corneum of human skin require development of higher-resolution terahertz tomography for industrial, medical, and cosmetic applications important. One of the most effective and simplest ways to improve the axial resolution of tomographic imaging is by generating broadband and short terahertz pulses using shorter optical pulses.

Practicality is also a critical issue in terahertz tomography. Most terahertz tomography systems heretofore reported use a Ti: sapphire laser as a pump light source because they meet stringent specifications and are suitable for generating and detecting terahertz pulses. However, for real applications in medical practices or factories, a more robust system that counteracts vibration and temperature variations is preferable. An ultrashort-pulse fiber laser would be a strong candidate, except for the belief that generating broadband ultrashort terahertz pulses with it would be difficult because its pulse width is longer than that of the Ti: sapphire laser. However, with the appropriate control of the nonlinear and dispersion effects in optical fibers, sub-20-fs optical pulses can be generated [8,9]. We have thus developed an all-fiber laser system that produces 17-fs optical pulses at a wavelength of 1.56 μm and have generated and detected broadband terahertz pulses ranging from 0.1 to 27 THz [10].

Here, we describe our high-resolution terahertz tomography system based on reflection-type THz-TDS. In this system, an all-fiber ultrashort-pulse laser is used to realize a system sufficiently robust for practical applications. To achieve a high resolution, broadband terahertz pulses generated using a 17-fs fiber laser and a DAST crystal are used as a terahertz source. Since the temporal waveform of the generated terahertz pulses has several multiple peaks, the deconvolution signal processing with Gaussian window is applied, which results in single-peaked and ultrashort terahertz pulses. Finally, the high-resolution of our system is demonstrated by successfully imaging a multilayered structure containing a 2-μm-thick GaAs layer.

The time-of-flight terahertz tomography experimental setup is shown in Fig. 1. Output pulses from a 1.56-μm fiber laser oscillator were fed into an erbium-doped fiber amplifier. The pulses were then compressed using a large mode-area photonic crystal fiber and a highly-nonlinear fiber [10]. The insert of Fig. 1 shows the temporal waveform of the compressed optical pulses. The average power, pulse width, and repetition frequency of the generated optical pulses were 200 mW, 17 fs, and 48 MHz, respectively.

The optical pulses were divided into two beams for terahertz wave generation and detection using a 50:50 broadband beam splitter. The terahertz waves were radiated from a 0.1-mm-thick DAST crystal. A germanium plate was inserted as a near-infrared filter to eliminate laser pulses transmitted through the crystal. The waves were collimated and focused onto the sample using a pair of 101.6-mm focal length parabolic mirrors whose location was optimized to achieve a minimum incident angle of 7°. The transverse resolution of the system was determined by the 0.9-mm spot size of the focused beam as measured by a knife-edge method. The terahertz pulses reflected from each layer of the sample were also focused on a 5-μm electrode gap LT-GaAs photoconductive antenna using parabolic mirrors. The temporal waveform of the terahertz waves was traced by scanning a delay stage whereby SHG pulses generated with a periodically-poled lithium niobate were used as probe pulses. The signal obtained was then fed into a preamplifier and detected with a lock-in amplifier. To reduce water vapor absorption effects during the tomography measurement, the terahertz wave path was purged with dry nitrogen gas.

Fig. 2(a) shows the temporal waveform of the detected terahertz pulses with a flat aluminum mirror used as an example. The inset shows the corresponding spectrum obtained by Fourier transforming the temporal waveform. The maximum amplitude is observed at 1 ps with several small oscillations superimposed on this peak. The corresponding spectrum extended

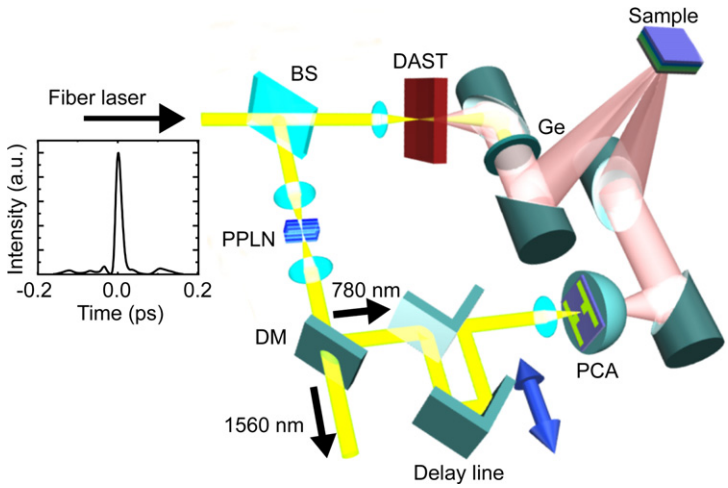

Fig. 1. Experimental setup for the fiber-laser, high-resolution time-of-flight terahertz tomography system. The inset shows the temporal waveform of the 17-fs fiber laser: BS: beam splitter; PPLN: periodically poled lithium niobate; DM: dichroic mirror; PCA: photoconductive antenna; Ge: germanium plate.

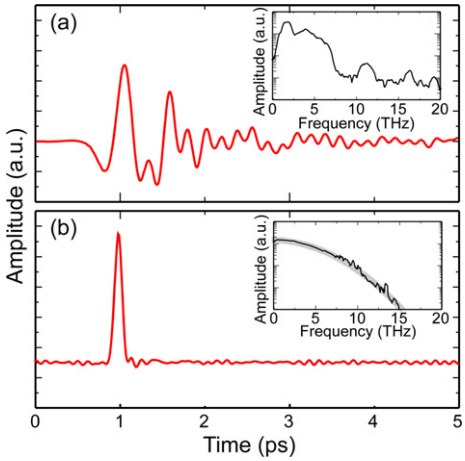

Fig. 2. Temporal waveform (a) as detected and (b) after signal processing. The inserts show the corresponding Fourier transforms. The gray curve represents a Gaussian-shaped waveform.

well beyond 20 THz; its trace is not flat due to either the absorption of the DAST crystal or phase mismatching. As shown in these figures, the temporal waveform of the detected terahertz pulses was distorted compared to those radiated from a photoconductive antenna. Signal processing is therefore required to suppress the tomographic ghost images and reshape the temporal waveform. In this work, the detected temporal waveform was analyzed using a deconvolution technique whereby the signal detected with another flat mirror was used as a reference. In addition, a Gaussian window function whose bandwidth was adjusted for a 100-fs temporal duration was used to suppress the sidelobes; the resultant temporal waveform is shown in Fig. 2(b). The corresponding spectrum is shown in the insert of Fig. 2(b) and has a Gaussian-like waveform. As shown in this figure, a single-peaked sidelobe-free pulse was obtained. A shorter pulse is obtained by broadening the Gaussian window bandwidth, but small side peaks arise in the temporal waveform due to an inverse relationship between temporal duration and sidelobe magnitude.

The Teflon film thickness was subsequently measured to evaluate the system's axial resolution. Fig. 3(a) shows the temporal waveform after the deconvolution process for a 12-μm-thick Teflon film sample. Two large peaks corresponding to the front and back sides of the film are clearly observed. These peaks have opposite signs due to phase inversion by reflection at the back of the film. The film thicknesses were calculated using the delay time of these peaks and the refractive index of the film. The experimental results obtained for several thicknesses of film are summarized in Fig. 3(b). The horizontal and vertical axes show the actual and measured thicknesses, respectively, where a 1-μm-resolution micrometer was used to measure the actual film thickness. In this figure, film thicknesses of 5, 12, 20, 25, and 30 μm were measured correctly. That is, the axial resolution is sufficient to measure 5-μm-thick Teflon film. Since the refractive index of the Teflon film is 1.9, the resolution of our system is less than $10/n$ μm, where n is the refractive index of the sample.

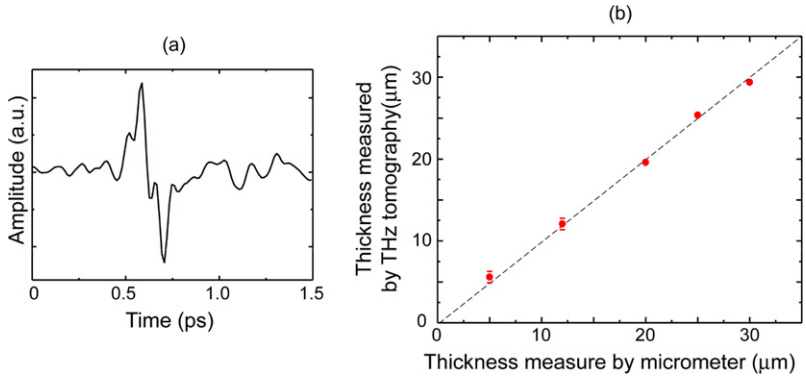

Fig. 3. Evaluation of axial resolution using Teflon films. (a) Typical measured temporal waveform and (b) measured thickness of Teflon films as a function of actual thickness. The actual thickness was measured using a micrometer.

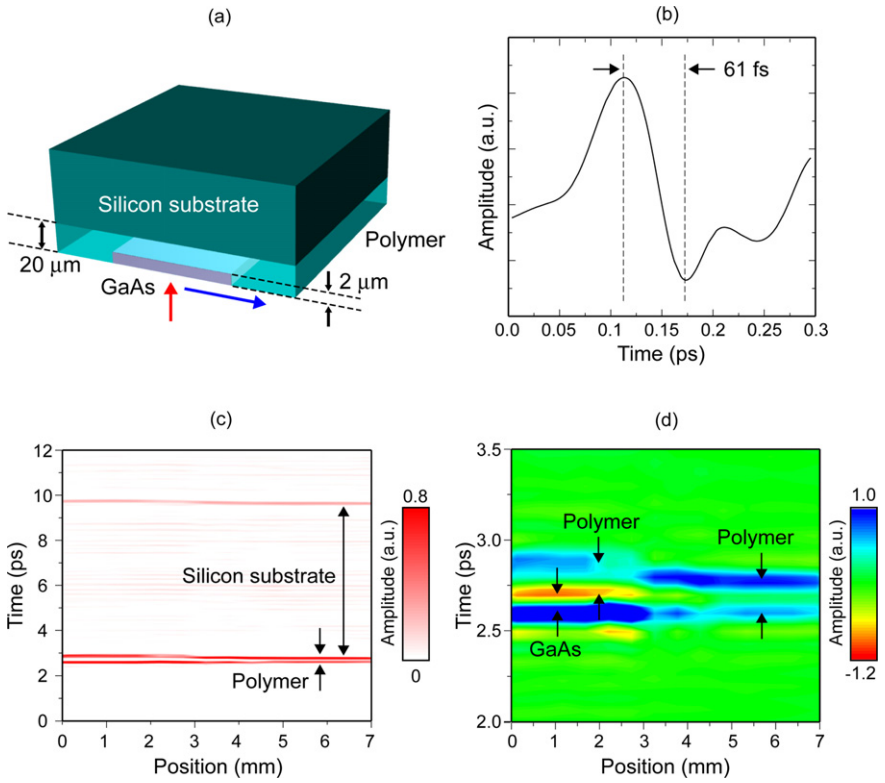

Fig. 4. Terahertz tomography of a semiconductor device sample: (a) schematic diagram of the sample, (b) temporal waveform obtained to measure the thickness of GaAs, (c) measured tomography image, and (d) close-up around the GaAs layer.

Lastly, terahertz tomography imaging was demonstrated. Fig. 4 shows terahertz tomography imaging of a semiconductor device. An approximately 2-μm GaAs layer was adhered to a 300-μm silicon substrate using a polymer resin; the schematic diagram of this device is shown in Fig. 4(a). The refractive indices of the GaAs layer, silicon substrate, and polymer resin at 1 THz are 3.6, 3.4, and 1.6, respectively. Fig. 4(b) shows the temporal waveform of the terahertz pulses obtained to measure the thickness of the GaAs layer, which is reflected from the point indicated by the red arrow. Since the GaAs layer had a larger refractive index than the polymer resin, the phase of the second peak was inverted. The time delay between these two peaks, which correspond to the front and reverse sides of the GaAs layer, was 61 fs. Taking the refractive index of GaAs into account, this time delay corresponds to a 2.5-μm-thick GaAs layer. Because the refractive index of the GaAs layer is about twice that of the Teflon film, the thickness of a layer thinner than that shown in Fig. 3(b) was also measured. However, the measured thickness may have been a little thicker than the estimated 2 μm, which is the resolution limit of our tomography system. Fig. 4(c) shows the 2D terahertz tomography image obtained by scanning the sample along the direction of the blue arrow. The silicon substrate and the polymer resin are obviously distinguished. Then, to confirm that

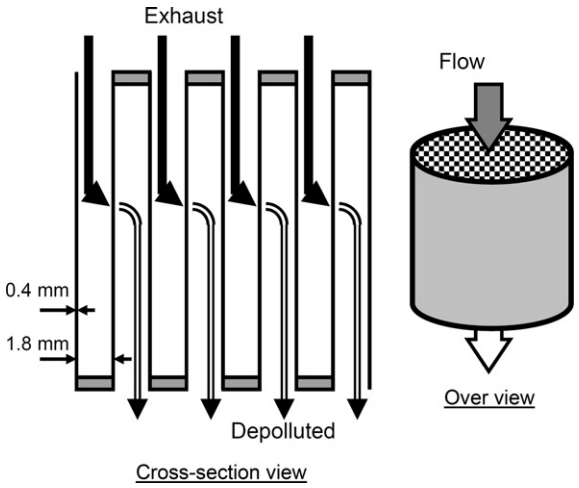

Fig. 5. The internal view (left) and the over view (right) of the soot removal filter. The exhaust emission gas is purified by passing though the 0.4-mm-thick ceramic walls, and is discharged into the atmosphere.

the thin GaAs layer was correctly imaged, the area around the GaAs layer was magnified and the color readjusted to more easily observe the thin layer as shown in Fig. 4(d). In this figure, the GaAs layer shown in Fig. 4(a) is observed at 0–3 mm.

3. Nondestructive inspection of an exhaust gas emission filter using computed tomography

Soot-trapping filters used as after-treatment systems for internal combustion engines may suffer loss of performance and/or failure due to the accumulation of soot. Sometime, the soot distribution in the filter becomes non-uniform, though there has been no method to visualize it. A nondestructive method of investigating the soot distribution would allow optimization of the filter. Here, we demonstrate a nondestructive computed tomography inspection system using millimeter-wave to terahertz radiation.

As shown in Fig. 5, the filter is comprised of ceramics in the form of many lattice cells. The soot is trapped by the micro-hole structure of the walls of the cells in the filter. It is necessary to remove the soot by heat-treatment because the performance of the internal combustion engine decreases as soot builds up. Avoiding decrease of the engine performance, frequent regeneration processes are needed, but this cause excessive fuel consumption. To not deteriorate the filter efficiency, damaged by excessive high temperature, we have to control the filter so as not to concentrate the soot accumulation highly in some area of it. Therefore, it is important to know how soot is distributed and how much soot accumulates in the filter. It is also highly desirable to be able do this in a nondestructive manner but there is no method.

The region of the electromagnetic spectrum in the millimeter wave (MMW) to terahertz (THz) wave is very attractive for advanced applications, due to the penetration into many non-metals. In the MMW region, sources with frequencies below 100 GHz are readily obtained, and have been used in commercially manufactured products such as collision-avoidance radar. In this study, we demonstrate the nondestructive inspection of soot distribution in the filter using a computed tomography (CT) technique, by exploiting the difference in the absorption coefficient between the soot and the filter. First, we select a suitable frequency for tomographic imaging by measuring the dependency of the transmittance on the angle of incidence of the electromagnetic radiation that originates in the filter's structure. Second, we measure the soot distribution in the filter using three-dimensional CT at the selected frequency.

The plan view of the filter is a lattice, as indicated in Fig. 5. When we measure the tomographic image, electromagnetic radiation is incident from the side, and a transmission image is acquired. There is a possibility that the transmitted radiation contains multiple reflections, which will result in a spectrum that is dependent on the incident angle of the radiation, because the periodicity of the structure (1.8 mm) is close to the wavelength of the MMW and THz-wave. The transmittance of the filter was measured within the frequency range from 30 GHz to 3 THz using THz-TDS, and the higher region above 300 GHz was almost opaque. It was measured as a function of the incident angle of the electromagnetic pulse at each frequency using a rotation stage.

We define the angle between the aspect of the wall, which makes grid pattern of the filter, and the direction of the electromagnetic radiation as θ. The light axis passes though the center of the filter. There is a strong dependence of the transmittance on the angle of incidence, resulting in behavior that is similar to that observed in photonic crystals. The angle-of-incidence—transmittance characteristics at 65, 80, 150, 175 and 250 GHz are shown in Fig. 6. There is a dip in the transmittance caused by the photonic band gap at high frequencies, whereas it is almost flat at 65 GHz. During CT imaging, a flat transmittance characteristic is preferable, as otherwise it would be necessary to de-convolve the dependence of the transmittance on the angle of incidence. Additionally, it is preferable to have a large transmittance, as this improves the signal-to-noise ratio. 65 GHz was chosen as the operating frequency of the CT system.

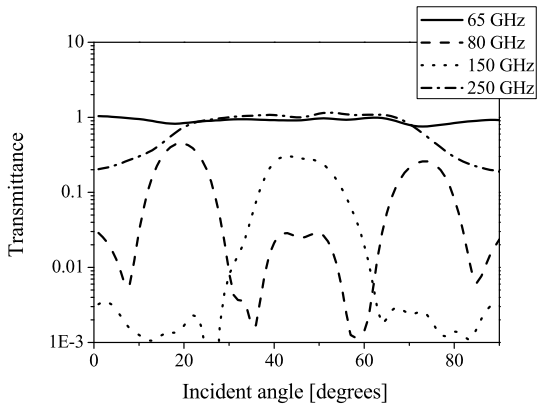

Fig. 6. The transmittance as a function of the angle of incidence at several frequencies. Strong fluctuations are only seen for the higher frequencies.

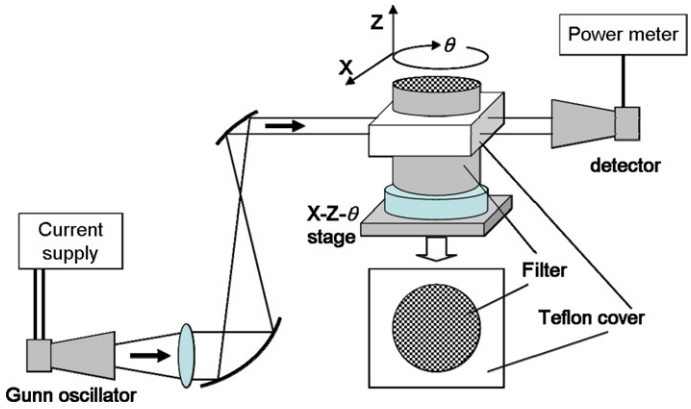

Fig. 7. Schematic diagram of the 3D-CT image acquisition system.

The CT imaging system is shown schematically in Fig. 7. A 65-GHz relaxation oscillator employing a Gunn diode was used as the source. The output from the relaxation oscillator was collimated using a horn antenna and a lens. The beam diameter (full-width at half-maximum) was reduced to 9.4 mm using two parabolic mirrors, and the sample (i.e., the soot filter) was placed on an X–Z–θ stage in the path of the collimated beam. Since the tested filter has a cylindrical shape, it behaves as a rod lens, and so was enclosed within a Teflon cover to prevent refraction at the interface with the air. As illustrated in Fig. 8, the distribution of soot in the filter which is made as test sample is non-uniform. The exhaust gas flows into the regions only shown by the black circles in the top-view in Fig. 8, and soot accumulates to a density of 4.7 g/L within the cylindrical regions of 110 mm in length. The final 40 mm of the filter does not contain any soot. A transmission image was recorded for a range of heights, shown in Fig. 8. The reconstructed image obtained using a two-dimensional inverse-Fourier transformation of the transmission images is shown in Fig. 9. The regions of accumulated soot can be clearly seen. The soot distribution in the X–Y plane can be confirmed, though the resolution of the image is little depleted. Some loss of resolution and distortion of the image occurs because of diffraction due to the mismatch of the refractive index of the filter and the Teflon cover, and due to artifacts of the inverse-Fourier transform.

4. Terahertz sensing of thin PET film thickness using a metallic mesh

In recent years, photonic crystals or metamaterials, which will likely be used as applications in many future optical devices because of their easy handling of electromagnetic waves, have attracted a great deal of attention [11]. We proposed a sensing and imaging method using 2D photonic-crystal “metallic-mesh” films in the THz region [12]. The transmission characteristics of metallic meshes, which have been investigated since the 1960s, are similar to those of far-infrared band-pass filters [13]. The metallic-mesh transmission properties, which depend on geometric parameters, such as the shape and size of the openings and the grid constant, have also been studied extensively [14]. This is because it has become easy to fabricate sophisticated, arbitrarily shaped metallic meshes inexpensively by processing techniques. The metallic-mesh transmission spectrum has long been known to be acutely affected by the refractive index of the material inside and above the metallic-mesh openings [15]. Using this phenomenon to our advantage, metallic-mesh sensing methods have been used for the detection of small amounts of proteins and for label-free detection of antigen–antibody reactions [16].

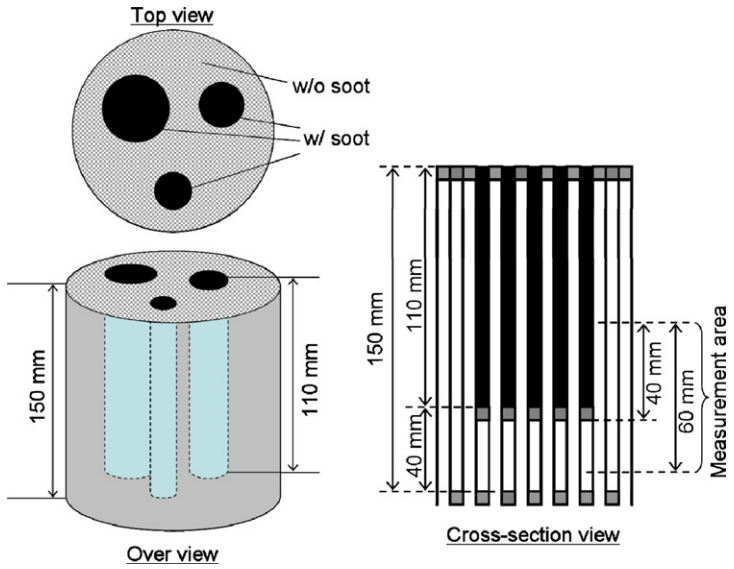

Fig. 8. Schematic diagram of the test sample of the soot removal filter. Soot accumulates in the three cylindrical areas with different radii.

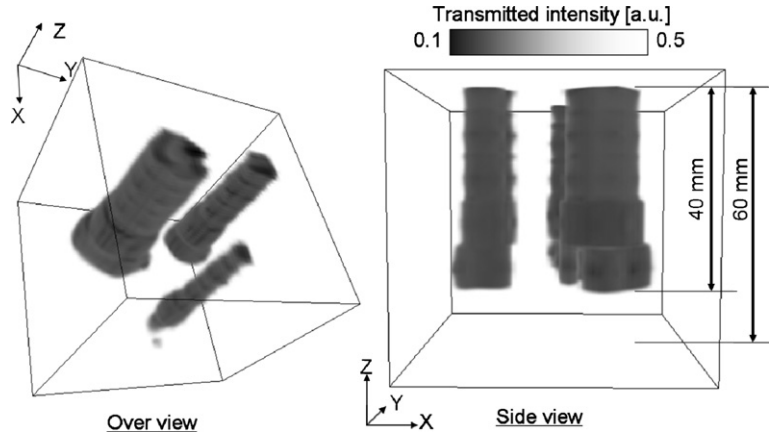

Fig. 9. The 3D-CT reconstruction image.

Here we successfully detected 3.5-μm-thick ultrathin PET films using the metallic-mesh sensing method by focusing our attention on the dip in the metallic-mesh transmission spectrum, which is due to a sudden change in transmittance. We also detected 1-μm-thickness differences in ultrathin PET films on the basis of 2D images of the transmittance. The metallic mesh used in our study has a 2D square lattice with square apertures. The structure is determined by the thickness, t, aperture size, a, and grating period, g. The metallic mesh behaves as a band-pass filter which has a transmission peak that is determined by the geometric parameters. The transmittance of the band-pass peak is resonantly enhanced and far higher than the opening ratio. This is referred to as anomalous transmission. This has been reported not only in the THz region but also for visible light [17]. The resonantly enhanced transmission is thought to be a composite effect caused by interference of the THz wave transmitted directly through the metal openings and the surface wave from the metal surface. Because of efficient reemission of surface waves from the backside of the metallic mesh, a far higher ratio of incident waves than the opening ratio seems to be supported by the metallic mesh [18]. A sudden change in transmittance, which we call the “dip”, appears in the high-transmittance region only when the THz wave is obliquely incident onto the metallic mesh.

We built an experimental system as shown in Fig. 10 to measure the transmission spectrum and to capture 2D images of the sample. We used a BWO (Backward Wave Oscillator) as the THz-wave source. This is a continuous-wave oscillator with a useful frequency from 0.9 to 1.1 THz. The THz wave from the BWO was reflected by an off-axis parabolic mirror and ITO (Indium Tin Oxide) glass, and was subsequently identified by a pyroelectric detector operating at room temperature. The diameter of the THz-wave focal point was 550 microns. Samples were placed at the focus position of the THz wave to measure their transmission properties. 2D images of the transmittance were also obtained by scanning the sample using an X–Y stage. The metallic mesh was made from Ni using an electroforming method. The geometric parameters of free-standing metallic mesh were $g = 254$ μm, $a = 180$ μm, and $t = 60$ μm.

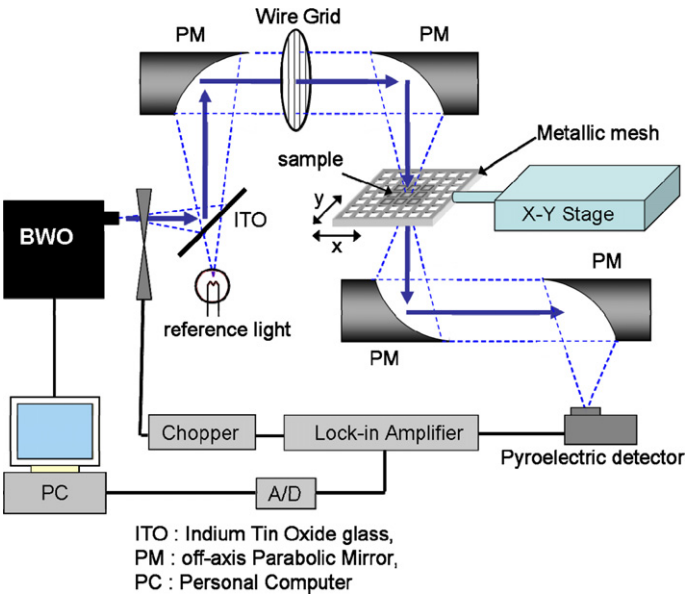

Fig. 10. Experimental system to measure the transmission spectrum and to obtain 2D images.

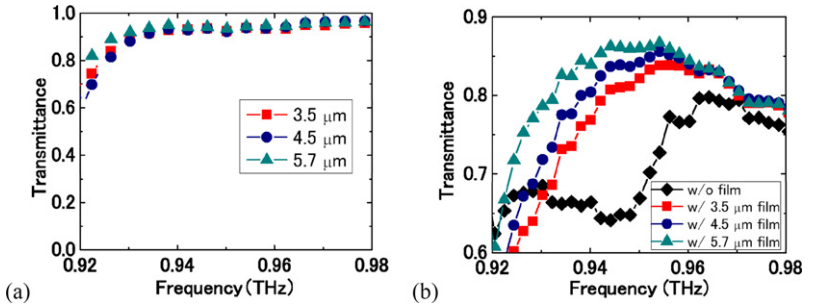

Fig. 11. (a) Transmission properties of ultrathin PET films without using metallic mesh. (b) Transmission spectrum of metallic mesh with and without PET films.

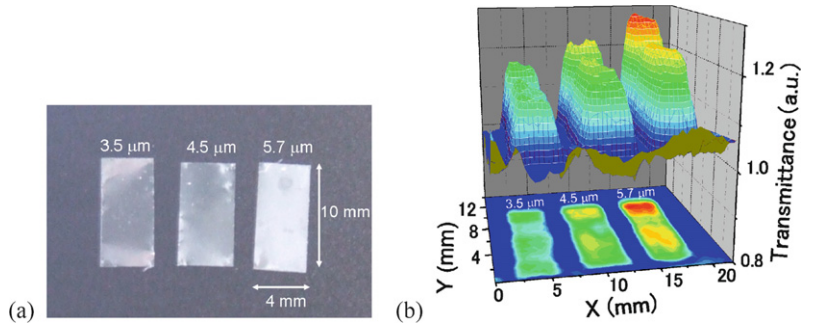

Fig. 12. Thickness-difference detection of ultrathin PET films using the metallic-mesh 2D imaging method. (a) Optical photograph of cut PET samples for 2D imaging. (b) 2D image of ultrathin PET films. The vertical axis is normalized to the transmittance of the metallic mesh without film.

The thicknesses of PET films were 3.5, 4.5, and 5.7 μm (Lumirror F53; Toray, Japan), which is about 100 times smaller than the THz wavelength of the BWO. As shown in Fig. 11(a), detecting differences in the THz-wave transmittance of these films was difficult without using metallic mesh. Therefore, we tried to detect the thickness differences of these films by using the metallic-mesh sensing method. Fig. 11(b) shows the experimental measurements of the metallic-mesh transmission properties with and without films. These films were held tightly to the metal surface by vacuuming up from the backside. The thickness differences of these films appeared as changes in the dip shifts of the metallic-mesh transmission properties. Next, we tried to capture 2D images of the PET films by scanning these films placed on the metal surface. Fig. 12(a) shows a photograph of the PET films with sizes of 4×10 mm. The frequency used to obtain the 2D image was 933 GHz,

given that the differences between the various transmittances appear evenly at this frequency. The 2D image at 933 GHz is shown in Fig. 12(b). Slight differences in ultrathin-film thickness compared to the THz-wave wavelength were shown as differences in transmittance in the 2D image. The transmittance was normalized to that of the metallic mesh without any film. Although they were placed on the same metallic mesh and hence should have been exactly the same, there are differences in transmittance in the *Y* direction appeared because these cut films could not adhere completely to the metallic-mesh surface.

5. Summary

We introduced several novel terahertz imaging techniques for industrial applications. First, the development of high-resolution time-of-flight terahertz tomography using a 17-fs fiber laser was presented. Broadband terahertz pulses obtained using a DAST crystal were injected into samples and the echo pulses reflected from each layer were detected. The deconvolution process then was carried out with a Gaussian window to obtain clean, high-resolution tomographic images. The high-resolution capability of our system provided the tomography images of multilayered structures built up of approximately 2-μm-thick layers. This high-resolution capability coupled with the practicality of an all-fiber-laser-based system will lead to further applications of terahertz tomography in the car paint inspection, etc.

Second, we have demonstrated measurement of the distribution of soot accumulations in a sample soot-trapping ceramic filter using MMW CT imaging. Three-dimensional CT images of the filter were acquired at 65 GHz, where there is no dependence of the transmittance on the angle of incidence. Using this technology, the design of filters with high collection efficiency of soot as well as the decision of regeneration timing with the least fuel consumption should be possible. By improving the optical system using a super-resolution algorithm, or deconvolution processing, more high-resolution images can be acquired.

Third, we studied on a metallic mesh affected by a sudden change in transmittance to develop a sensing or imaging method with high sensitivity in the THz region. Using this metallic-mesh sensing method, we succeeded in detecting 1-μm-thickness differences in ultrathin PET films, which is about 300 times thinner than a THz-wave wavelength. By scanning these samples in two-dimensions, we also detected the varied thicknesses as the differences in transmittance in the 2D image. We will try to improve the sensitivity of the sensing method by optimizing the experimental system and the structure of the metallic mesh.

Acknowledgements

Authors would like to express a great gratitude to Dr. Jun Takayanagi, Dr. Eiji Kato, Dr. Masatsugu Yamashita, Dr. Chiko Otani, Prof. Yuichi Ogawa, Prof. Norihiko Nishizawa, Dr. Hideyuki Ohtake, Dr. Toshihiko Ouchi, Dr. Shintaro Kasai, Mr. Hirohisa Uchida, Prof. Koichiro Tanaka and Prof. Hiromasa Ito, for their collaborations. This work was partly supported by funded researches from companies and a Grant-in-Aid for Scientific Research (18206009) from the Ministry of Education, Culture, Sports, Science and Technology (MEXT), Japan.

References

[1] M. Tonouchi, Cutting-edge terahertz technology, Nature Photonics 1 (2007) 97–105.
[2] D.M. Mittleman, R.H. Jacobsen, M.G. Nuss, T-ray imaging, IEEE J. Sel. Top. Quantum Electron. 2 (1996) 679–692.
[3] D.M. Mittleman, et al., T-ray tomography, Opt. Lett. 22 (1997) 904–906.
[4] T. Yasui, et al., Terahertz paintmeter for noncontact monitoring of thickness and drying progress in a paint film, Appl. Opt. 44 (2005) 6849–6856.
[5] A.J. Fitzgerald, B.E. Cole, P.F. Taday, Nondestructive analysis of tablet coating thickness using terahertz pulsed imaging, J. Pharm. Sci. 94 (2005) 177–183.
[6] D. Huang, et al., Optical coherence tomography, Science 254 (1991) 1178–1181.
[7] J.L. Johnson, T.D. Dorney, D.M. Mittleman, Enhanced depth resolution in terahertz imaging using phase-shift interferometry, Appl. Phys. Lett. 78 (2001) 835–837.
[8] Y. Matsui, M.D. Pelusi, A. Suzuki, Generation of 20-fs pulses from a gain-switched laser diode by a four-stage soliton compression technique, IEEE Photon. Technol. Lett. 11 (1999) 1217–1219.
[9] T. Hori, N. Nishizawa, T. Goto, Generation of 14 fs ultrashort pulse in all fiber scheme by use of highly nonlinear hybrid fiber, in: T. Kobayashi, et al. (Eds.), Ultrafast Phenomena XIV, Springer-Verlag, Berlin, 2005, pp. 31–33.
[10] J. Takayanagi, et al., Generation and detection of broadband coherent terahertz radiation using 17-fs ultrashort pulse fiber laser, Opt. Express 16 (2008) 12859–12865.
[11] A.K. Azad, et al., Effect of dielectric properties of metals on terahertz transmission in subwavelength hole arrays, Opt. Lett. 31 (2006) 2637–2639.
[12] F. Miyamaru, et al., Terahertz surface-wave resonant sensor with a metal hole array, Opt. Lett. 31 (2006) 1118–1120.
[13] R. Ulrich, Far-infrared properties of metallic mesh and its complementary structure, Infrared Phys. 7 (1967) 37–55.
[14] C.C. Chen, Transmission of microwave through perforated flat plates of finite thickness, IEEE Trans. Microwave Theory Tech. MTT-21 (1973) 1–6.
[15] M. Tanaka, et al., Effect of a thin dielectric layer on terahertz transmission characteristics for metal hole arrays, Opt. Lett. 30 (2005) 1210–1212.
[16] H. Yoshida, et al., Terahertz sensing method for protein detection using a thin metallic mesh, Appl. Phys. Lett. 91 (2007) 253901.
[17] T.W. Ebbesen, et al., Extraordinary optical transmission through sub-wavelength hole arrays, Nature 391 (1998) 667–669.
[18] M. Sarrazin, J.P. Vigneron, J.M. Vigoureux, Role of Wood anomalies in optical properties of thin metallic films with a bidimensional array of subwavelength holes, Phys. Rev. B 67 (2003) 085415.